Article

# Desalination Performance of MoS$_2$ Membranes with Different Single-Pore Sizes: A Molecular Dynamics Simulation Study

Bin Wu, Zailing Song, Yuanyi Xiang, Haili Sun, Haiyun Yao, and Junlang Chen*

Cite This: *ACS Omega* 2024, 9, 22851−22857

Read Online

ACCESS | 📊 Metrics & More | 📖 Article Recommendations | 🗄 Supporting Information

**ABSTRACT:** Utilizing molecular dynamics simulations, we examined how varying pore sizes affect the desalination capabilities of MoS$_2$ membranes while keeping the total pore area constant. The total pore area within a MoS$_2$ nanosheet was maintained at 200 Å$^2$, and the single-pore areas were varied, approximately 20, 30, 40, 50, and 60 Å$^2$. By comparing the water flux and ion rejection rates, we identified the optimal single-pore area for MoS$_2$ membrane desalination. Our simulation results revealed that as the single-pore area expanded, the water flux increased, the velocity of water molecules passing the pores accelerated, the energy barrier decreased, and the number of water molecules within the pores rose, particularly between 30 and 40 Å$^2$. Balancing water flux and rejection rates, we found that a MoS2 membrane with a single-pore area of 40 Å$^2$ offered the most effective water treatment performance. Furthermore, the ion rejection rate of MoS$_2$ membranes was lower for ions with lower valences. This was attributed to the fact that higher-valence ions possess greater masses and radii, leading to slower transmembrane rates and higher transmembrane energy barriers. These insights may serve as theoretical guidance for future applications of MoS$_2$ membranes in water treatment.
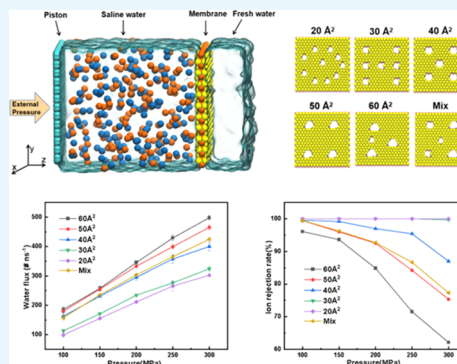
## 1. INTRODUCTION

Two-dimensional (2D) materials are widely used in the fields of conductive substrates,[1−3] filter membranes,[4−6] and energy storage[7−9] because of their unique structures and excellent performance. Membranes made of 2D materials have excellent properties, such as large specific surface areas, high adsorption capacities, and high separation efficiencies, and have good prospects for application in water treatment.[10−23] One typical 2D material is molybdenum disulfide (MoS$_2$), from which nanofiltration membranes with excellent desalination performance are prepared, and their advantages in water treatment are gradually emerging.[24−28] For example, Li et al. prepared atomic-thick MoS$_2$ membranes using chemical vapor deposition.[27] The membranes have a high desalination capacity with high rejection rates (>99%) of Na$^+$, K$^+$, Ca$^{2+}$, and Mg$^{2+}$, as well as a high water flux (>322 L m$^{-2}$ h$^{-1}$ bar$^{-1}$).[29] Sapkota et al. reported single- and double-layer thick MoS$_2$ films as porous mesh structures with a tunable surface charge, pore size, and interlayer spacing. These porous nano-MoS$_2$ films are capable of efficient rejection of organic dye molecules and ions and have excellent durability to chlorine exposure.[30]

Computationally, using molecular dynamics (MD) simulations, Heiranian et al. found that the water flux of MoS$_2$ membranes is 2−5 orders of magnitude higher than those of other nanoporous membranes. They constructed three MoS$_2$ nanopores, i.e., pores with only molybdenum atoms at the edge, only sulfur atoms, and both molybdenum and sulfur atoms, and found that the pores with only molybdenum atoms at the edge had higher water fluxes (approximately 70% higher

than those of graphene nanopores).[31] Subsequently, Heiranian et al. evaluated the application and capability of molecular simulations in comprehending the mechanisms involved in ion and water transport across polymeric membranes.[32] Cao et al. also compared the water treatment effects of different 2D materials. They found that the water flux of a monolayer of MoS$_2$ was consistently 27% higher than that of graphene, 38% higher than that of phosphorus, 35% higher than that of boron nitride, and 20% higher than that of molybdenum diselenide with the same pore size of these 2D materials.[33] Kou et al. used MD simulations to construct nanoporous MoS$_2$ monolayers with different pore radii ranging from 5.3 to 13.5 Å. Their simulation results indicated that a nanoporous MoS$_2$ membrane with a pore radius of 7.4 Å had a high water flux and a perfect desalination rate.[34] The fast movement of water molecules in the monolayer MoS$_2$ nanopores was attributed to the single hydrogen bonding chain connecting the water molecules inside and outside the nanopores. Similarly, Azamat and Khataee designed four MoS$_2$ nanopores of different areas (9.306 to 37.345 Å$^2$) to filter heavy-metal ions. They found
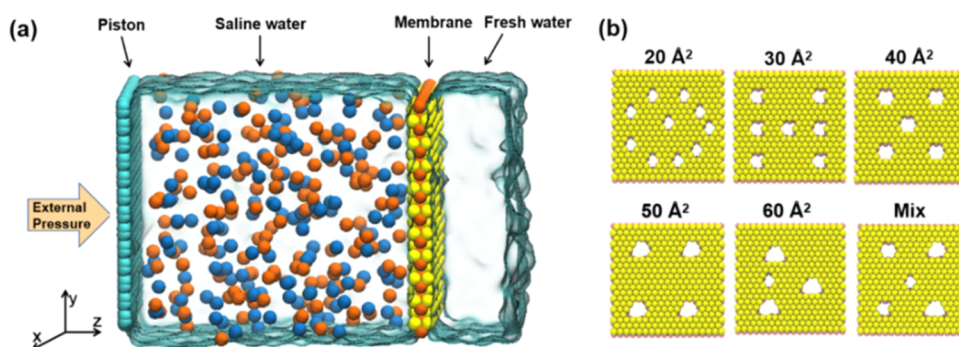
**Figure 1.** (a) Side view of a single simulated system consisting of a piston, a pore-containing monolayer $MoS_2$ membrane, and two water boxes. The water box on the left contains brine, and the box on the right contains pure water. (b) Atomic structures of $MoS_2$ membranes with different pore areas. Color scheme for panel (a): Mo, yellow; S, orange; C, cyan; $Na^+$, red; and $Cl^-$, blue.

that a membrane with a pore area of 22.423 $Å^2$ could completely retain heavy-metal ions and had a high water flux.[35]

Despite the excellent desalination performance of pore-containing $MoS_2$ membranes, the relationships between their water fluxes and ion rejection rates and the size and number of pores need to be further investigated. In this study, MD simulations were used to explore the effects of different single-pore areas on the desalination performance when the total pore area was kept constant. We sought to identify an ideal pore size with high water flux and reasonable ion rejection rate (more than 90%)[36,37] by varying the single-pore area and the total pore area remaining fixed. In addition, considering the diversity of ion valence, we investigated the desalination performance of pore-containing $MoS_2$ membranes for solutions containing monovalent sodium ions ($Na^+$), divalent calcium ions ($Ca^{2+}$), and trivalent iron ions ($Fe^{3+}$).

## 2. SIMULATION METHODS

Figure 1(a) shows the structure of a single simulated system with a box size of $4 \times 4 \times 13$ $nm^3$, which can be divided into four parts from left to right: the graphene piston, brine solution ($NaCl/CaCl_2/FeCl_3$) with a concentration of 1.0 mol/L, $MoS_2$ monolayer containing nanopores, and pure water box. The $MoS_2$ monolayer was constructed using the Visual Molecular Dynamics software.[38] With the total pore area set as approximately 200 $Å^2$, five different pore areas were constructed: 20 $Å^2$ (10 pores), 30 $Å^2$ (7 pores), 40 $Å^2$ (5 pores), 50 $Å^2$ (4 pores), and 60 $Å^2$ (3 pores plus an 20 $Å^2$ pore), as shown in Figure 1(b). The area of the pores was formed by removing atoms. A hybrid porous $MoS_2$ monolayer (labeled "Mix") was also constructed as control, which consisted of five pores with areas of 20, 30, 40, 50, and 60 $Å^2$, for a total hole area of 200 $Å^2$.

All MD simulations were conducted by the LAMMPS software.[39] The water molecules were modeled by the SPC/E model,[40] and the SHAKE algorithm with an accuracy tolerance of 0.0001 was used to constrain the bond lengths and bond angles of the water molecules. The van der Waals and electrostatic interactions between atoms were calculated by using the Lennard−Jones (LJ) potential and long-range Coulomb interactions, respectively. The LJ parameters for the pairwise interactions in the system are presented in Table S1 (see Supporting Information, Table S1). The interactions between different atoms were calculated by using the Lorentz− Berthelot mixing rule. The truncation radii for both the LJ potential and Coulomb interactions were 12 Å, and the long-range Coulomb interactions were calculated using the

particle−particle−particle grid solver with a relative root-mean-square error of 0.005.

The simulation process consisted of three steps: (i) energy minimization, (ii) NPT process, and (iii) NVT simulation. First, 10,000 iterations were performed for energy minimization. Then, the simulation was performed via NPT ensemble with a step size of 1 fs, using the Nosé−Hoover heat bath method for temperature and pressure regulation, with a temperature of 300 K, pressure of 1 bar, and simulation time of 100 ps.[41,42] During the equilibrium period, the $MoS_2$ atoms were kept fixed in space, and the NPT simulation brought the water to equilibrium density (1 $g/cm^3$). Finally, the desalination process was simulated under NVT ensemble with 2 fs steps, a temperature of 300 K, a simulation time of 10 ns, and an extrapolation pressure of 100−300 MPa. The external pressure was achieved by applying a force along the $z$-axis to each atom in the piston. The force $F$ was calculated by the following equation

$$F = \frac{pS}{N}$$

where $p$ represents the externally applied pressure, $S$ represents the area of the piston, and $N$ represents the total number of atoms in the piston.

The water flux and rejection rate were calculated by using the counting function of the LAMMPS software, which gives the number of ions and oxygen atoms passing through the membrane. The water flux (WF) was given as

$$WF = \frac{N_w}{T}$$

where WF represents the water flux, $N_w$ represents the number of water molecules passing through the membrane, and $T$ represents the simulation time.

The ion rejection rate ($R$) equation was

$$R = \frac{N_{ion} - N_{ion1}}{N_{ion}}$$

where $R$ represents the rejection rate, $N_{ion}$ represents the total number of ions, and $N_{ion1}$ represents the number of ions passing through the membrane.

## 3. RESULTS AND DISCUSSION

**3.1. Water Fluxes and Rejection Rates of $MoS_2$ Membranes with Different Single-Pore Areas.** Water flux is one of the most important indicators of nanofiltration
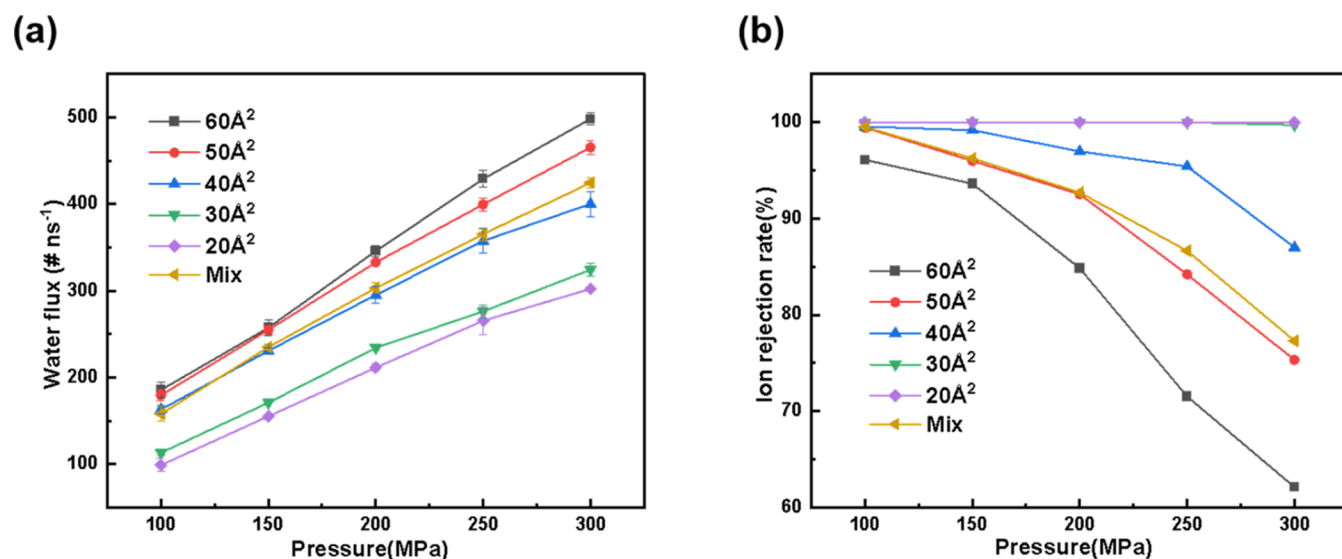
**Figure 2.** (a) Water fluxes and (b) ion rejection rates for six membranes with different pore areas under applied pressure.
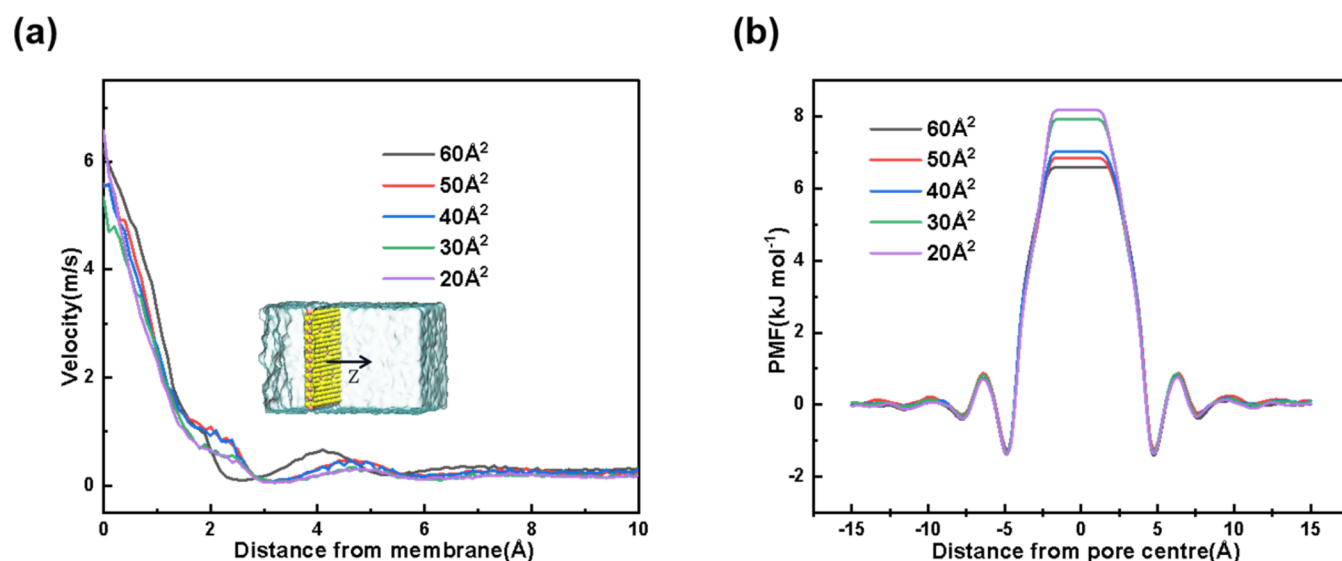


**Figure 3.** (a) Transmembrane velocity of water molecules; (b) PMF of water molecules passing through the pores.

membranes, as shown in Figure 2(a). At pressures of 100−300 MPa, the water flux increased approximately linearly with the increasing pressure. For single-pore areas ranging from 20 to 60 $Å^2$, the $MoS_2$ membrane with a single-pore area of 60 $Å^2$ exhibited the highest water flux among all of the membranes, followed by the $MoS_2$ membranes with single-pore areas of 50, 40, 30, and 20 $Å^2$. The water flux of the hybrid pore membrane, which was given by the average value for the five pore areas, was close to that of the 40 $Å^2$ pore membrane. The variations in the water flux from 20 to 30, 40 to 50, and 50 to 60 $Å^2$ were smaller than that from 30 to 40 $Å^2$. For example, at an external pressure of 250 MPa, the water flux for a single-pore area of 30 $Å^2$ was 4.09% higher than that for a single-pore area of 20 $Å^2$, and the water flux for a single-pore area of 60 $Å^2$ was 9.49% higher than that for a single-pore area of 50 $Å^2$. However, the water flux for a single-pore area of 40 $Å^2$ was surprisingly 29.40% higher than that for a single-pore area of 30 $Å^2$, and the water fluxes at other pressures exhibited similar results.

Another important parameter related to desalination performance is ion rejection, which indicates the ability of the membrane to filter ions, as shown in Figure 2(b). The relevant data is presented in Tables S2 and S3 (see Supporting Information, Tables S2 and S3). Typically, the ion rejection rate decreases with an increase in pressure because high pressures exert stronger forces on ions, causing more ions to pass through the pores. For example, for a single-pore area of 60 $Å^2$, the rejection rate decreased from 95.13 to 63.96% when the pressure was increased from 100 to 300 MPa, and for a single-pore area of 50 $Å^2$, the rejection rate decreased from 99.45 to 75.33% when the pressure was increased from 100 to 300 MPa. For the 20 and 30 $Å^2$ pores, the rejection rate was almost 100% regardless of the exerted pressure. For example, the rejection rate was 99.70% only for the single-pore area of 30 $Å^2$ at an external pressure of 300 MPa. For the 40 $Å^2$ pore, the rejection rate slightly declined with increasing external pressure. However, even at a pressure of 200 MPa, the rejection rate was still as high as 96.97%. For the hybrid pore, the rejection rate was close to that of a single-pore area of 50

$Å^2$, for example, 92.70% for the hybrid pore and 92.53% for the 50 $Å^2$ pore at 200 MPa.

**3.2. Velocities and Potential of Mean Forces of Water Molecules Passing through Pores.** To further understand the effects of the single-pore area on the water flux of $MoS_2$ membranes, we analyzed the transmembrane velocity and potential of mean force (PMF) of water molecules. The velocity and PMF of water molecules in the z-direction in five pores were examined at 200 MPa. As shown in Figure 3(a), the velocity of water molecules varied generally with changes in the single-pore area. The normal velocities (along the z-axis) at the membrane surface for pores with areas of 60, 50, 40, 30, and 20 $Å^2$ were recorded as 5.76, 5.59, 5.54, 5.34, and 6.57 m/s, respectively. Notably, the velocity for the largest pore size (60 $Å^2$) was slightly higher than those observed for the smaller pore sizes (50, 40, and 30 $Å^2$). This can be attributed to the fact that a larger pore area facilitates the passage of water molecules, resulting in a higher velocity. However, this trend was unexpectedly disrupted for the smallest pore size (20 $Å^2$). Surprisingly, the velocity recorded for the 20 $Å^2$ pores was 14.06% higher than that for the 60 $Å^2$ pores. This anomaly can be explained by the fact that the smaller pores, despite their size, experience a concentrated pressure when subjected to the same overall pressure. As a result, when water molecules successfully pass through these narrow pores, they move at a significantly higher speed. This finding highlights the complex interplay among pore size, pressure, and water flux in $MoS_2$ membranes.

The PMF of water molecules passing through the pore-containing $MoS_2$ membrane is shown in Figure 3(b). The PMF is given by the equation $F(r) = -RT \ln[\rho(r)]$, where $R$ is the molar gas constant, $T$ represents the temperature, $r$ represents the distance from the membrane, and $\rho$ denotes the density of water at the membrane. The highest energy barrier was encountered by water molecules passing through the 20 $Å^2$ pore, and the energy barrier decreases as the pore size increases. Both the speed of water molecules across the membrane (except for the 20 $Å^2$ pore) and the water flux increased as the pore size increased, which makes sense since a lower energy barrier leads to faster velocity and higher water flux. Furthermore, a significant decrease in the energy-barrier height was observed when the area of a single pore was enlarged from 30 to 40 $Å^2$, indicating that the membrane with a 40 $Å^2$ pore area offers optimal conditions for the passage of water molecules. Generally, a larger pore area facilitates the movement of water molecules, resulting in slightly lower energy barriers for the 50 and 60 $Å^2$ pores. The PMF profiles provide insight into the relationship between the water fluxes of $MoS_2$ membranes with different single-pore areas and the transmembrane energy barriers that water molecules encountered. Specifically, smaller pore areas correlate with higher energy barriers, leading to a reduced number of water molecules passing through.

**3.3. Number Densities of Na⁺ Ions near the Pores.** Considering the effects of the number density of ions on the rejection rate, we plotted the number density curves in the range of 15 Å on the membrane surface at 200 MPa (Supporting Information, Table S4). As shown in Figure 4, the ion number densities had obvious peaks on the membrane surface, and all of the peaks of 20, 30, 40, and 50 $Å^2$ pores were almost located at the same position ($z = 7$ Å). Correspondingly, the peaks of the ion number density were 0.0038, 0.0040, 0.0044, and 0.0050 ions/$Å^3$. That is to say, with the increase of
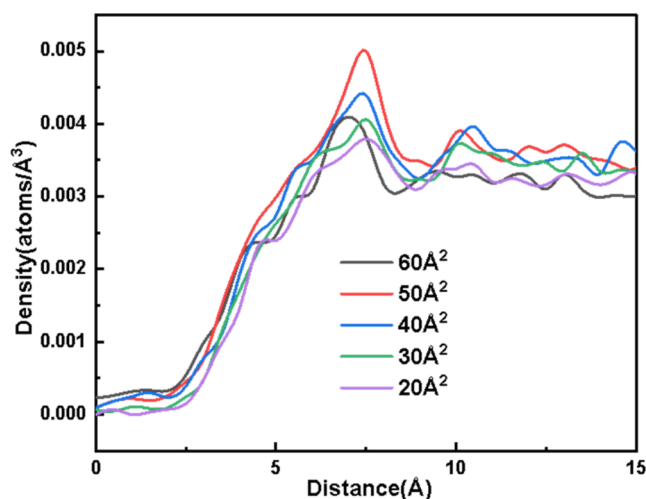


**Figure 4.** Number density of Na⁺ ions near the pores.

pore area, more ions will appear around the membrane, making ions more likely to pass through the pores, which leads to a decrease in the rejection rate. However, the $MoS_2$ membrane with a single-pore area did not follow the above trend from 50 to 60 $Å^2$, and its ion number density did not continue to increase with an increase in the single-pore area; rather, it decreased to a value similar to that of 30 $Å^2$ (0.0038 ions/$Å^3$). Because the 60 $Å^2$ pores had a low ion rejection capacity, ions passed through them faster and did not remain on the membrane surface, and the lower ion rejection capacity made it more difficult to form ion number density peaks on the membrane surface.

**3.4. Water Fluxes and Rejection Rates of Solutions Containing Different Valence Ions.** To simulate a system closer to the real water environment, we investigated the effects of ionic valence on the desalination of $MoS_2$ membranes. This was done by replacing the 1.0 mol/L NaCl solution with 1.0 mol/L $CaCl_2$ and $FeCl_3$ solutions at a fixed pressure of 200 MPa. The overall trend of the water fluxes of the solutions with different valence ions was $Na^+ > Ca^{2+} > Fe^{3+}$. The water fluxes of the solutions with $Na^+$, $Ca^{2+}$, and $Fe^{3+}$ were 295.23, 209.67, and 159.13 #ns⁻¹, respectively, at a single-pore area of 40 $Å^2$. As shown in Figure 5(a), the water flux increased with a single-pore area. For example, the water flux of the $Na^+$ solution increased by 26.06% from 30 to 40 $Å^2$, whereas that of the $Ca^{2+}$ solution increased by only 6.70%. For the $Fe^{3+}$ solution, the single-pore area hardly affected the water flux, and the water fluxes of 20, 30, 40, 50, and 60 $Å^2$ pores were 157.6, 161.1, 159.1, 143.9, and 164.9 #ns⁻¹, respectively. In addition to the water flux, we investigated the rejection rates of the five membranes for different ions. Figure 5(b) shows the percentages of ions of different valence states blocked by the five nanomembranes. The general trend of the ion rejection rates was $Na^+ < Ca^{2+} < Fe^{3+}$. For example, at a single-pore area of 40 $Å^2$, the rejection rates of $Na^+$, $Ca^{2+}$, and $Fe^{3+}$ were 96.97, 99.00, and 99.76%, respectively. In general, the ion rejection rate decreases with an increase in the pore area because with a larger pore area there is more space for ions to pass through. For example, the ion rejection rate of $Ca^{2+}$ decreased from 99.00 to 90.50% as the single-pore area increased from 40 to 60 $Å^2$. Compared with the other two ions, the $MoS_2$ membrane exhibited high rejection rates for $Fe^{3+}$, with 99.5% rejection even at a single-pore area of 50 $Å^2$.
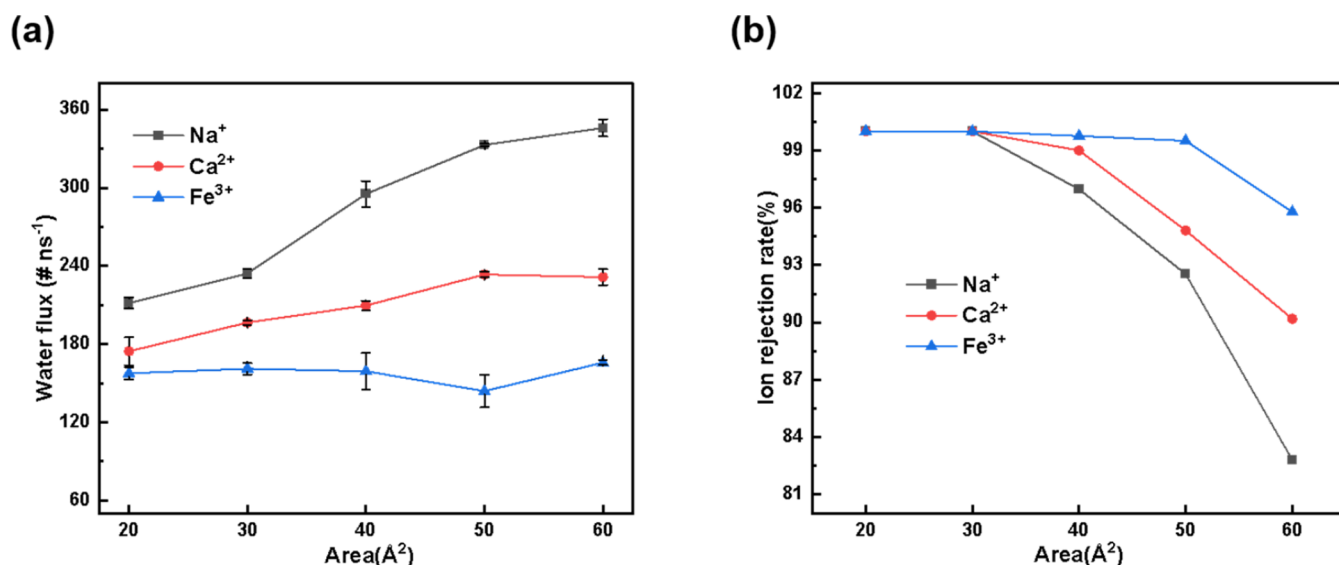
**(a)**



**(b)**

**Figure 5.** (a) Water fluxes and (b) ion rejection rates of five membranes with different pore areas for different valence ions.
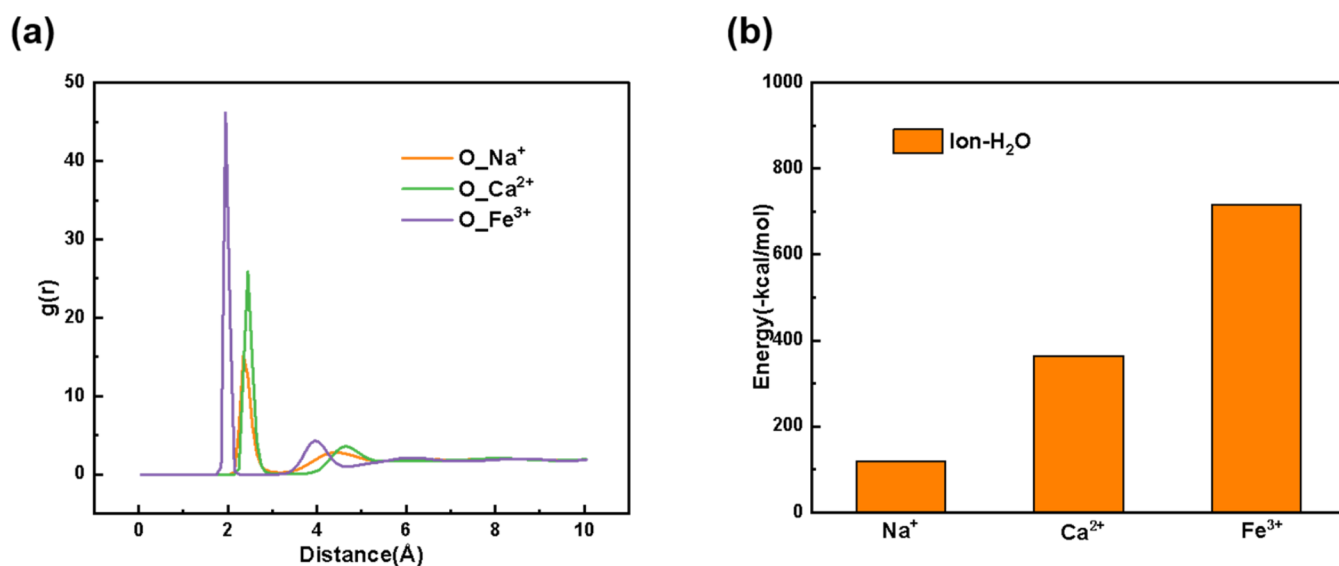
**(a)**



**(b)**

**Figure 6.** (a) Radial distributions of different ions with respect to oxygen atoms of water molecules; (b) binding energies of different ions to water molecules.

To explore the underlying mechanisms of how ion valence affects water flux and rejection rates, we analyzed the interactions between water molecules and ions. Specifically, we characterized these interactions through the radial distributions and binding energies of ions to water molecules. As depicted in Figure 6(a), all three ions, namely $Fe^{3+}$, $Ca^{2+}$, and $Na^+$, formed hydrated layers. For instance, $Fe^{3+}$ exhibited distinct first and second hydrated layers positioned at distances of 1.95 and 3.95 Å, respectively, whereas $Ca^{2+}$ formed its hydrated layers at distances of 2.45 and 4.65 Å. Furthermore, Figure 6(b) presents the binding energies between cations ($Na^+$, $Ca^{2+}$, and $Fe^{3+}$) and water molecules. Notably, the binding energy between $Fe^{3+}$ and water molecules was the highest, reaching −715.82 kcal/mol. This energy was approximately 1.96 times greater than the binding energy between $Ca^{2+}$ and water and nearly 6.01 times higher than that between $Na^+$ and water. This significant difference suggests that the binding between $Fe^{3+}$ and water is significantly more stable compared to the hydrated states of $Na^+$ and $Ca^{2+}$. On

the other hand, the hydration of ions with water molecules increases their masses, thereby reducing their mobility and diffusion velocities. This decrease in movement directly leads to a lower water flux. Additionally, hydrated ions exhibit enlarged radii, resulting in the high rejection rates. Consequently, this explains the observed trend where the water flux follows the order of $Na^+ > Ca^{2+} > Fe^{3+}$, while the ion rejection rate follows the inverse order of $Na^+ < Ca^{2+} < Fe^{3+}$.

## 4. CONCLUSIONS

In summary, we conducted molecular dynamics simulations to assess the water fluxes and ion rejection rates of nanoporous $MoS_2$ membranes, varying the single-pore areas from 20 to 60 Å$^2$ while maintaining a constant total pore area of 200 Å$^2$. The simulation results are summarized as follows: First, the water flux escalated with the increase in the single-pore area, particularly when it expanded from 30 to 40 Å$^2$. This was attributed to the rise in the normal velocity of water molecules and the corresponding reduction in the transmembrane energy

barrier. Second, the number density of ions adjacent to the pores rose with the increasing single-pore area, leading to a decline in ion rejection rates. Third, lower-valence ions exhibited higher water fluxes and lower ion rejection rates in $MoS_2$ membranes. This was due to the larger masses and radii of hydrated higher-valence ions, which slowed their trans-membrane rates and increased the transmembrane energy barriers. Considering both the rejection rates and water fluxes, our results suggest that a $MoS_2$ membrane with a single-pore area of 40 Å$^2$ may be the most effective for water desalination. Our findings could serve as theoretical insights for future feasibility studies exploring the application of $MoS_2$ pore-containing film materials in water treatment.

## ASSOCIATED CONTENT

### Ⓢ Supporting Information

The Supporting Information is available free of charge at https://pubs.acs.org/doi/10.1021/acsomega.4c01208.

> LJ parameters used in the simulation; water fluxes for six membranes with different pore areas under applied pressures from 100 to 300 MPa; rejection rates for six membranes with different pore areas under applied pressures from 100 to 300 MPa; number densities of $Na^+$ ions near the pores (PDF)

## AUTHOR INFORMATION

### Corresponding Author

**Junlang Chen** − *College of Mathematics and Computer Science, College of Optical, Mechanical and Electrical Engineering, Zhejiang A&F University, Hangzhou 311300, China;* ⓞ orcid.org/0000-0001-9238-781X;
Email: chenjunlang7955@sina.com

### Authors

**Bin Wu** − *College of Mathematics and Computer Science, College of Optical, Mechanical and Electrical Engineering, Zhejiang A&F University, Hangzhou 311300, China*

**Zailing Song** − *College of Mathematics and Computer Science, College of Optical, Mechanical and Electrical Engineering, Zhejiang A&F University, Hangzhou 311300, China;* ⓞ orcid.org/0009-0000-2632-3148

**Yuanyi Xiang** − *Radiation Monitoring Technical Center of Ministry of Ecology and Environment, State Environmental Protection Key Laboratory of Radiation Monitoring, Key Laboratory of Radiation Monitoring of Zhejiang Province, Hangzhou 310012, China*

**Haili Sun** − *Zhejiang GuoFu Environmental Technology Co., Ltd, Hangzhou 311300, China*

**Haiyun Yao** − *Radiation Monitoring Technical Center of Ministry of Ecology and Environment, State Environmental Protection Key Laboratory of Radiation Monitoring, Key Laboratory of Radiation Monitoring of Zhejiang Province, Hangzhou 310012, China*

Complete contact information is available at:
https://pubs.acs.org/10.1021/acsomega.4c01208

### Notes

The authors declare no competing financial interest.

## REFERENCES

(1) Barakzehi, M.; Montazer, M.; Sharif, F.; Norby, T.; Chatzitakis, A. A Textile-based Wearable Supercapacitor Using Reduced Graphene Oxide/Polypyrrole Composite. *Electrochim. Acta* **2019**, *305*, 187−196.

(2) Li, L.; Zhang, N.; Zhang, M.; Zhang, X.; Zhang, Z. Flexible Ti3C2Tx/PEDOT:PSS films with outstanding volumetric capacitance for asymmetric supercapacitors. *Dalton Trans.* **2019**, *48*, 1747−1756.

(3) Khan, A. H.; Ghosh, S.; Pradhan, B.; Dalui, A.; Shrestha, L. K.; Acharya, S.; Ariga, K. Two-Dimensional (2D) Nanomaterials towards Electrochemical Nanoarchitectonics in Energy-Related Applications. *Bull. Chem. Soc. Jpn.* **2017**, *90*, 627−648.

(4) Shannon, M. A.; Bohn, P. W.; Elimelech, M.; Georgiadis, J. G.; Mariñas, B. J.; Mayes, A. M. Science and Technology for Water Purification in the Coming Decades. *Nature* **2008**, *452*, 301−310.

(5) Wang, L.; Boutilier, M. S. H.; Kidambi, P. R.; Jang, D.; Hadjiconstantinou, N. G.; Karnik, R. Fundamental Transport Mechanisms, Fabrication and Potential Applications of Nanoporous Atomically Thin Membranes. *Nat. Nanotechnol.* **2017**, *12*, 509−522.

(6) Cohen-Tanugi, D.; McGovern, R. K.; Dave, S. H.; Lienhard, J. H.; Grossman, J. C. Quantifying the Potential of Ultra-permeable Membranes for Water Desalination. *Energy Environ. Sci.* **2014**, *7*, 1134−1141.

(7) Lukatskaya, M. R.; Kota, S.; Lin, Z.; Zhao, M.-Q.; Shpigel, N.; Levi, M. D.; Halim, J.; Taberna, P.-L.; Barsoum, M. W.; Simon, P.; Gogotsi, Y. Ultra-high-rate Pseudocapacitive Energy Storage in Two-dimensional Transition Metal Carbides. *Nat. Energy* **2017**, *2*, No. 17105.

(8) Dong, Y.; Zheng, S.; Qin, J.; Zhao, X.; Shi, H.; Wang, X.; Chen, J.; Wu, Z.-S. All-MXene-Based Integrated Electrode Constructed by Ti3C2 Nanoribbon Framework Host and Nanosheet Interlayer for High-Energy-Density Li−S Batteries. *ACS Nano* **2018**, *12*, 2381−2388.

(9) Zhang, X.; Hou, L.; Ciesielski, A.; Samorì, P. 2D Materials Beyond Graphene for High-Performance Energy Storage Applications. *Adv. Energy Mater.* **2016**, *6*, No. 1600671.

(10) Khawaji, A. D.; Kutubkhanah, I. K.; Wie, J.-M. Advances in Seawater Desalination Technologies. *Desalination* **2008**, *221*, 47−69.

(11) Ghaffour, N.; Missimer, T. M.; Amy, G. L. Technical Review and Evaluation of the Economics of Water Desalination: Current and Future Challenges for Better Water Supply Sustainability. *Desalination* **2013**, *309*, 197−207.

(12) Celebi, K.; Buchheim, J.; Wyss, R. M.; Droudian, A.; Gasser, P.; Shorubalko, I.; Kye, J.-I.; Lee, C.; Park, H. G. Ultimate Permeation Across Atomically Thin Porous Graphene. *Science* **2014**, *344*, 289−292.

(13) Martí, J.; Sala, J.; Guàrdia, E. Molecular Dynamics Simulations of Water Confined in Graphene Nanochannels: From Ambient to Supercritical Environments. *J. Mol. Liq.* **2010**, *153*, 72−78.

(14) Sun, L.; Ying, Y.; Huang, H.; Song, Z.; Mao, Y.; Xu, Z.; Peng, X. Ultrafast Molecule Separation through Layered WS2 Nanosheet Membranes. *ACS Nano* **2014**, *8*, 6304−6311.

(15) Lei, W.; Portehault, D.; Liu, D.; Qin, S.; Chen, Y. Porous Boron Nitride Nanosheets for Effective Water Cleaning. *Nat. Commun.* **2013**, *4*, No. 1777.

(16) Zhang, Y.; Su, K.; Li, Z. Graphene Oxide Composite Membranes Cross-linked with Urea for Enhanced Desalting Properties. *J. Membr. Sci.* **2018**, *563*, 718−725.

(17) Huang, H.-H.; Joshi, R. K.; De Silva, K. K. H.; Badam, R.; Yoshimura, M. Fabrication of Reduced Graphene Oxide Membranes for Water Desalination. *J. Membr. Sci.* **2019**, *572*, 12−19.

(18) Qin, S.; Liu, D.; Wang, G.; Portehault, D.; Garvey, C. J.; Gogotsi, Y.; Lei, W.; Chen, Y. High and Stable Ionic Conductivity in

2D Nanofluidic Ion Channels between Boron Nitride Layers. *J. Am. Chem. Soc.* **2017**, *139*, 6314−6320.

(19) Cohen-Tanugi, D.; Lin, L.-C.; Grossman, J. C. Multilayer Nanoporous Graphene Membranes for Water Desalination. *Nano Lett.* **2016**, *16*, 1027−1033.

(20) Liu, H.; Wang, H.; Zhang, X. Facile Fabrication of Freestanding Ultrathin Reduced Graphene Oxide Membranes for Water Purification. *Adv. Mater.* **2015**, *27*, 249−254.

(21) Kazemi, A. S.; Abdi, Y.; Eslami, J.; Das, R. Support Based Novel Single Layer Nanoporous Graphene Membrane for Efficacious Water Desalination. *Desalination* **2019**, *451*, 148−159.

(22) Russo, C. J.; Golovchenko, J. A. Atom-by-atom Nucleation and Growth of Graphene Nanopores. *Proc. Natl. Acad. Sci. U.S.A.* **2012**, *109*, 5953−5957.

(23) Zhang, L. L.; Zhao, X.; Stoller, M. D.; Zhu, Y.; Ji, H.; Murali, S.; Wu, Y.; Perales, S.; Clevenger, B.; Ruoff, R. S. Highly Conductive and Porous Activated Reduced Graphene Oxide Films for High-Power Supercapacitors. *Nano Lett.* **2012**, *12*, 1806−1812.

(24) Wang, Z.; Mi, B. Environmental Applications of 2D Molybdenum Disulfide (MoS2) Nanosheets. *Environ. Sci. Technol.* **2017**, *51*, 8229−8244.

(25) Sun, L.; Huang, H.; Peng, X. Laminar MoS2Membranes for Molecule Separation. *Chem. Commun.* **2013**, *49*, 10718−10720, DOI: 10.1039/c3cc46136j.

(26) Feng, J.; Graf, M.; Liu, K.; Ovchinnikov, D.; Dumcenco, D.; Heiranian, M.; Nandigana, V.; Aluru, N. R.; Kis, A.; Radenovic, A. Single-layer MoS2 Nanopores as Nanopower Generators. *Nature* **2016**, *536*, 197−200.

(27) Li, H.; Ko, T.-J.; Lee, M.; Chung, H.-S.; Han, S. S.; Oh, K. H.; Sadmani, A.; Kang, H.; Jung, Y. Experimental Realization of Few Layer Two-Dimensional MoS2Membranes of Near Atomic Thickness for High Efficiency Water Desalination. *Nano Lett.* **2019**, *19*, 5194−5204.

(28) Li, W.; Yang, Y.; Weber, J. K.; Zhang, G.; Zhou, R. Tunable, Strain-Controlled Nanoporous MoS2 Filter for Water Desalination. *ACS Nano* **2016**, *10*, 1829−1835.

(29) Li, Y.; Yang, S.; Zhang, K.; Van der Bruggen, B. Thin Film Nanocomposite Reverse Osmosis Membrane Modified by Two Dimensional Laminar MoS2 with Improved Desalination Performance and Fouling-resistant Characteristics. *Desalination* **2019**, *454*, 48−58.

(30) Sapkota, B.; Liang, W.; VahidMohammadi, A.; Karnik, R.; Noy, A.; Wanunu, M. High Permeability Sub-nanometre Sieve Composite MoS2Membranes. *Nat. Commun.* **2020**, *11*, No. 2747.

(31) Heiranian, M.; Farimani, A. B.; Aluru, N. R. Water desalination with a single-layer MoS2 nanopore. *Nat. Commun.* **2015**, *6*, No. 8616.

(32) Heiranian, M.; DuChanois, R. M.; Ritt, C. L.; Violet, C.; Elimelech, M. Molecular Simulations to Elucidate Transport Phenomena in Polymeric Membranes. *Environ. Sci. Technol.* **2022**, *56*, 3313−3323.

(33) Cao, Z.; Liu, V.; Farimani, A. B. Why is Single-Layer MoS2 a More Energy Efficient Membrane for Water Desalination? *ACS Energy Lett.* **2020**, *5*, 2217−2222, DOI: 10.1021/acsenergylett.0c00923.

(34) Kou, J.; Yao, J.; Wu, L.; Zhou, X.; Lu, H.; Wu, F.; Fan, J. Nanoporous Two-dimensional MoS2Membranes for Fast Saline Solution Purification. *Phys. Chem. Chem. Phys.* **2016**, *18*, 22210−22216.

(35) Azamat, J.; Khataee, A. Improving the Performance of Heavy Metal Separation from Water Using MoS2Membrane: Molecular Dynamics Simulation. *Comput. Mater. Sci.* **2017**, *137*, 201−207.

(36) Yang, Z.; Wu, C.; Tang, C. Y. Making waves: Why do we need ultra-permeable nanofiltration membranes for water treatment? *Water Res.: X* **2023**, *19*, No. 100172, DOI: 10.1016/j.wroa.2023.100172.

(37) Lyu, J.; Wen, X.; Kumar, U.; You, Y.; Chen, V.; Joshi, R. K. Separation and purification using GO and r-GO membranes. *RSC Adv.* **2018**, *8*, 23130−23151.

(38) Humphrey, W.; Dalke, A.; Schulten, K. Visual Molecular Dynamics. *J. Mol. Graphics* **1996**, *14*, 33−38.

(39) Plimpton, S. Fast Parallel Algorithms for Short-Range Molecular Dynamics. *J. Comput. Phys.* **1995**, *117*, 1−19.

(40) Mark, P.; Nilsson, L. Structure and Dynamics of the TIP3P, SPC, and SPC/E Water Models at 298 K. *J. Phys. Chem. A* **2001**, *105*, 9954−9960.

(41) Hoover, W. G. Canonical Dynamics: Equilibrium Phase-space Distributions. *Phys. Rev. A* **1985**, *31*, 1695−1697.

(42) Nosé, S. A Unified Formulation of the Constant Temperature Molecular Dynamics Methods. *J. Chem. Phys.* **1984**, *81*, 511−519.